Granite rock fragmentation at percussive drilling - experimental and numerical investigation

M. Saadati[a,b], P. Forquin[c], K. Weddfelt[b], P.L. Larsson[a,*], F. Hild[d]

[a] *Department of Solid Mechanics, KTH Royal Institute of Technology , Stockholm, Sweden*

[b] *Atlas Copco, Örebro, Sweden*

[c] *3SR Lab., Joseph Fourier University, Grenoble, France*

[d] *LMT Cachan, ENS Cachan / CNRS / UPMC / PRES UniverSud Paris, Cachan, France*

Abstract

The aim of this study is to numerically model the fracture system at percussive drilling. Due to the complex behavior of rock materials, a continuum approach is employed relying upon a plasticity model with yield surface locus as a quadratic function of the mean pressure in the principal stress space coupled with an anisotropic damage model. In particular, Bohus granite rock is investigated and the material parameters are defined based on previous experiments. This includes different tests such as direct tension and compression, three point bending and quasi-oedometric tests to investigate the material behavior at both tension and confined compression stress states. The equation of motion is discretized using a FE approach and the explicit time integration method is employed. EOI (Edge-On Impact) tests are performed and the results are used to validate the numerical model. The percussive drilling problem is then modeled in 3D and the bit-rock interaction is considered using contact mechanics. The fracture mechanism in the rock and the bit penetration- resisting force response are realistically captured by the numerical model.

Keywords: Granite, percussive drilling, KST-DFH model, fragmentation

[*]Corresponding author
Email address: plla@kth.se

1 Introduction

Rock drilling has been extensively used in the mining industry for many decades. A sound understanding of bit-rock interaction and rock fragmentation mechanisms is essential to optimize the drilling process. The percussive drilling method is commonly used in the tunneling and mining business. The main idea is that a piston hits the drill rod at a velocity of about 10 m/s. This creates a compressive stress wave with an amplitude of about 200 MPa, which propagates along the drill rod. The stress wave is then transferred into the rock through the tool buttons. Each tool includes around ten buttons made of hard steel that facilitate the indentation process. Unlike the situation of quasi-static indentation, the stress waves and rapid indentation make percussive drilling a transient dynamic problem with high local strain rates in the rock [1].

Basic defects in rocks are voids, pores and microcracks as well as other related features [2]. Such microstructures produce heterogeneity in the strength and stiffness of the material. It is well known that rock fractures via initiation, growth and coalescence of microcracks, together with sliding between individual grains and the microcrack surfaces. Associated with these microscopic mechanisms, rock specimens exhibit non-linear stress-strain responses [2]. Granite, which is the material studied in this work, has many pre-existing cracks, (e.g. [3] and [4]), but the porosity is very low (about 0.2%). Most rocks show a transition from brittle to ductile behavior by increasing the confined pressure [2]. However, silicate rocks with low porosity are brittle at room temperature over the whole range of normal laboratory confining pressures up to 0.5-1.0 GPa. Some workers have reported that granite exhibits brittle fracture behavior even at confining pressures up to 3-4 GPa [5].

Many studies have been performed during the past years to numerically simulate rock drilling and the fragmentation process in brittle materials. Liu [6] developed a rock and tool interaction code (R-T^{2D}) and studied the fragmentation process in a quasi-static situation. Wang et al. [7] used an in-house numerical tool to simulate the rock fragmentation process induced by indentation. Both Liu and Wang et al. restrict their analyses to 2D plain strain conditions and do not account for inelastic strains. Furthermore, Saksala [8,9] studied the impact indentation of rocks using an isotropic damage concept for tensile loading and a viscoplasticity consistency model for compression loading. This work is performed under 2D plane strain conditions. More recently, the model was extended to deal with 3D simulations [10]. Chiang et al. [11] modeled the impact of tool to the rock and rock fragmentation in drilling process using a 3D FE approach. A linear Mohr envelop together with a tension cut off plane is employed as a criterion for maximum strength of rock. The material behavior is considered linear elastic before reaching the final failure. Additionally, Thuro et al. [12] used Particle Flow Code (PFC^{2D}) to investigate the crack pattern in drilling and its correlation with existing foliations. PFC^{2D} code is based on discontinuum mechanics approach and is built for 2D simulations.

Forquin and Hild [13] studied dynamic fragmentation in brittle materials in general due to impact loading by using a probabilistic approach to describe the material behavior. The constitutive equation consists of the plasticity model introduced by Krieg [14], Swenson and Taylor [15] for compressive loadings and coupled with the anisotropic damage model developed by Denoual and Hild [16], Forquin and Hild [13], in tension (here and in the sequel referred to as the KST-DFH model). It is shown how a brittle and

random behavior under quasi-static tensile loading becomes deterministic and stress-rate dependent when increasing the loading rate. This type of model was able to describe the fragmentation of two grades of limestone subjected to EOI tests [17] and the enhancement of strength and failure pattern of a microconcrete [18] and a standard concrete [19] in spalling tests and EOI experiments.

In this investigation, the KST-DFH model is selected as the constitutive model based on the findings in a previous study by Saadati et al [20]. This model is a good alternative as it deals with both dynamic fragmentation due to tensile stress waves and also plasticity-like deformation in compression. This is very similar to the situation at percussive drilling as the impact of the piston induces stress waves into the rock and initiate tensile cracks, while high compressive stresses prevail beneath the indenter and lead to crushing of the rock. The KST-DFH model parameters for Bohus granite are defined based on previously reported experimental results [20]. Edge-On Impact (EOI) tests, i.e. impact of an aluminum projectile onto a rock slab [21], are performed. The tests are numerically modeled and these results are compared to the experimental data to validate the constitutive model. After that, the numerical tool is used to simulate the percussive drilling problem and the results are compared with real drilling data.

2 Constitutive specification

2.1 KST model

The KST model has been developed to simulate the compressive behavior of geomaterials accounting for the effect of hydrostatic and deviatoric parts of the stress tensor [14,15]. In the deviatoric part, the locus of the yield surface is a quadratic function of the mean pressure in the principal stress space.

$$\sigma_{eq} = \sqrt{a_0 + a_1 P + a_2 P^2} \tag{1}$$

where σ_{eq} is the equivalent (von Mises) stress, P the hydrostatic stress, a_0, a_1 and a_2 are material dependent coefficients.

Furthermore, the model includes a piece-wise linear equation of state linking the volumetric strain, ε_v, to the hydrostatic stress. At the first stage of hydrostatic loading, the material behaves elastically. By increasing the pressure, collapse of pores occurs in the case of porous rocks, which is modeled by an irreversible volumetric strain. During the porosity breakage, the bulk modulus, K, decreases noticeably. When all pores are closed, the material exhibits a higher bulk modulus which corresponds to the compacted material [22]. However, granite exhibits constant bulk modulus in the whole hydrostatic stress range as it includes a very small amount of porosity [20].

2.2 The DFH fragmentation model

The DFH fragmentation model is explained in detail in Refs. [13] and [16]. In the sequel a brief summary of the model including both single and multiple fragmentation regimes is presented.

2.2.1 Single fragmentation

Under low loading rate conditions, the fracture process is generally the consequence of the initiation and growth of a single crack. When the stress increases, the weakest defect is first activated. An unstable crack is initiated and propagates very quickly leading to fracture of the whole structure.

Defects with different sizes and orientations are randomly distributed within the material and consequently the failure stress is random. To model this tensile behavior, a probabilistic approach may be employed. Using a Poisson point-process framework, the weakest link theory and Weibull model, the failure probability P_F is given by [23,24]

$$P_F = 1 - \exp[-Z_{eff}\,\lambda_t(\sigma_F)] \tag{2}$$

where Z_{eff} is the effective volume [25], and λ_t is the initiation density defined by

$$\lambda_t(\sigma_F) = \lambda_0 \left(\frac{\sigma_F}{S_0} \right)^m \tag{3}$$

where m is the Weibull modulus, S_0^m / λ_0 is the Weibull scale parameter, and σ_F the maximum principal stress in the whole domain. The effective volume, Z_{eff}, is expressed as

$$Z_{eff} = ZH_m \tag{4}$$

where Z is the size of the whole volume, and H_m the stress heterogeneity factor [26] written as

$$H_m = \frac{1}{Z} \int_\Omega \left(\frac{\langle \sigma_1 \rangle}{\sigma_F} \right)^m dZ \text{ when } \sigma_F > 0 \tag{5}$$

where σ_1 is the local maximum principal stress, and $\langle \bullet \rangle$ Macauley's brackets. The stress heterogeneity factor characterizes the effect of the load pattern on the cumulative failure probability. Last, the average failure stress σ_w and the corresponding standard deviation σ_{sd} are written as

$$\sigma_w = S_0 (\lambda_0 Z H_m)^{-1/m} \Gamma\left(1 + \frac{1}{m}\right) \tag{6}$$

and

$$\sigma_{sd} = S_0 (\lambda_0 Z H_m)^{-1/m} \sqrt{\Gamma\left(1 + \frac{2}{m}\right) - \Gamma^2\left(1 + \frac{1}{m}\right)} \tag{7}$$

where Γ is the Euler function of the second kind

$$\Gamma(1 + x) = \int_0^\infty \exp(-u) u^x du \tag{8}$$

To characterize specific materials, 3-point bend tests are performed and the distribution of the failure stresses is obtained. One classical way to obtain the Weibull modulus m is then to look at the slope of linear interpolation in the diagram of $\ln[-\ln(1-P_F)]$ versus $\ln(\sigma_F)$ or the modified Weibull plot [20]. The scale parameter S_0^m / λ_0 can then be extracted from Eqs. (6) and (8), or the intercept in the Weibull plot.

2.2.2 Multiple fragmentation

Under high strain-rate conditions, several cracks are initiated and propagate from the initial defects leading to multiple fragmentation. The initial defects are assumed to be randomly distributed and activated for a random level of stress. When a crack is initiated, it propagates at a very high velocity (a portion of the stress wave velocity) and relaxes the stresses in its vicinity. This prevents activation of new defects in an obscured zone centered on this crack. At the same time the stress is increasing in the non-obscured zone and new critical defects are activated leading to new crack openings [13,16].

Therefore, dynamic fragmentation corresponds to a competition between, on the one hand, new critical defects that progressively initiate cracks with the increase of the stress level and, on the other hand, obscuration of areas of potential critical defects by cracks created before. The fragmentation process ends when the whole domain is obscured by the propagating cracks.

The interaction law between cracks already initiated and the critical defects of the material is given by the concept of probability of non-obscuration [16]. If the initiation density is a continuous function, the probability of non-obscuration of point M at time T in a domain Ω is described by [13]

$$P_{no}(M,T) = \exp\left(- \iint\limits_{(x,t)\in[\,horizon\ of\ (M,T)]} \frac{\partial \lambda_t(x,t)}{\partial t} dV dt \right) \tag{9}$$

where the horizon is defined by

$$horizon\ of\ (M,T) = \{x,t\} \in [Z_o(T-t) = S(kC(T-t))^n \cap \Omega]. \tag{10}$$

In Eq. (10), Z_o is the obscured zone, k a constant parameter (k = 0.38 when the crack length becomes significantly larger than the initial size), C the 1D wave speed, T the current time and t the crack initiation time, S a shape parameter (equal to $4\pi/3$ when the obscuration volume is similar to a sphere in 3D) and n the medium dimension (n = 3 in 3D).

The single fragmentation process occurs at quasi-static conditions and the probability of obscuration $P_o = 1 - P_{no} \equiv P_F$ corresponds to the failure probability, Eq.(2), expressed by Weibull's model. Therefore the initiation density for dynamic fragmentation (see Eq. (9)) is identical to that used in the analysis of quasi-static cases as described in Eq.

(3).

In the case of multiple fragmentation, the interaction between the horizon and the boundary of the domain Ω is small and if a uniform stress field is assumed, the obscuration probability in multiple fragmentation is written as [16]

$$P_o(T) = 1 - P_{no}(T) = 1 - \exp\left(-\int_0^T \frac{d\lambda_t}{dt} [\sigma(t)]\, Z_o(T-t) dt \right) \tag{11}$$

The non-obscuration probability provides an indication for the fraction of initiated cracks that correspond to the critical defects activated in the non-obscured volumes. The increment of the crack density λ_{cracks} is associated with the obscuration probability and the increment of initiation density

$$\frac{\partial \lambda_{cracks}}{dt} = P_{no} \frac{\partial \lambda_t}{dt} \tag{12}$$

Eq. (12) expresses the fact that cracks will initiate only if a defect exists in a non-obscured zone of the volume. The probability of obscuration is defined for each principal direction i and the evolution of P_i is expressed in a differential form in order to be employed in a FE code using Eq. (11)

$$\frac{d^2}{dt^2}\left(\frac{1}{1-P_i}\frac{dP_i}{dt}\right) = 3!S\left(kC_0\right)^3 \lambda_t[\sigma_i(t)] \; when \; \frac{d\sigma_i}{dt} > 0 \; and \; \sigma_i > 0 \tag{13}$$

where σ_i is the local principal stress component.

The KST-DFH model is also combined with a cohesive model in order to describe the cohesive strength in the obscured zone and the softening behavior of geomaterials in dynamic tension [27]. In the cohesive model, an extra term is added to the macroscopic stress Σ_i as

$$\Sigma_i = (1-P_i)\sigma_i + (P_i)^{\alpha_D}\sigma_{coh}(\varepsilon) = (1-D_i)\sigma_i \tag{14}$$

where σ_{coh} is the residual strength in the obscuration zone

$$\sigma_{coh} = \sigma_o^d \exp\left(-\left(\frac{\varepsilon}{\varepsilon_0^d}\right)^{n_d}\right) \tag{15}$$

where α_D, σ_o^d, ε_o^d, n_d are material-dependent parameters, and D_i the damage variable defined for each principal direction. The cohesive term can be seen as an extra contribution related to the fracture energy of the material. It enforces the final failure of an element to occur when the dissipated energy due to the damage process reaches the fracture energy of the material.

In the principal stress frame, the compliance tensor is defined by

$$\begin{bmatrix} \varepsilon_1 \\ \varepsilon_2 \\ \varepsilon_3 \end{bmatrix} = \frac{1}{E}\begin{bmatrix} \frac{1}{1-D_1} & -\nu & -\nu \\ -\nu & \frac{1}{1-D_2} & -\nu \\ -\nu & -\nu & \frac{1}{1-D_3} \end{bmatrix}\begin{bmatrix} \Sigma_1 \\ \Sigma_2 \\ \Sigma_3 \end{bmatrix} \tag{16}$$

where ε_1, ε_2, ε_3 are the principal strains, E Young's modulus and ν Poisson's ratio of the undamaged material. At the inception of damage growth, the principal damage frame coincides with the principal

stress tensor frame and the eigen directions may change at each time step until the first damage variable D_1 reaches a threshold value of 0.2. Then the direction of D_1 is locked and the other directions D_2, and D_3 follow the eigen directions with the constraint to be perpendicular to D_1. When the second damage variable reaches the threshold value, the whole directions are locked.

3 The material model parameters

The KST-DFH model parameters for Bohus granite, see Table legends

Table 1, are obtained based on previous experimental work [20]. In Table legends

Table 1, the mechanical properties (E and ν) are determined from direct tensile and compression tests while the DFH model parameters are obtained mainly from flexural experiments. The KST model is calibrated based on quasi-oedometric test results, see Figure legends

Fig. 1, and in particular the experimental data at high levels of hydrostatic pressure for which there is a considerable amount of inelastic strains (as the specimen mainly deforms elastically at the initial stage of loading). Presently, the equation of state linking the volumetric strain to the hydrostatic stress is taken to be piece-wise linear and determined by the points ($\varepsilon_v^{(i)}$, $P^{(i)}$) specified in Table legends

Table 1.

It deserves to mention that in the model, rate dependency is negligible in case of single fragmentation and the strength of the material is then considered to be probabilistic. At higher stress rates (i.e. when multiple fragmentation occurs) the mechanical behavior is deterministic and the strength increases with increasing loading rates. At low stress-rates, Weibull law plays also a regularization role. The smaller the FE elements the higher the mean failure stress based on Weibull size effect. Furthermore, the rate dependency at high stress rates works as a regularization in the model and decreases mesh dependency. More details concerning this behavior are found in Ref. [13].

The parameters of the cohesive law are here determined based on preliminary results from spall tests. All the material parameters used hereafter are summarized in Table legends

Table 1.

4 Edge-on impact experiments and computations

4.1 Experiments

In order to validate the numerical model and also to investigate the fracture pattern after impact, Edge-on Impact (EOI) tests [21] with a special sarcophagus configuration [16] are performed (see Fig. 2). In the experimental set-up, two cylindrical steel confinements of size 52 mm in length and 60 mm in diameter are used close to the impact point on both faces of the rock specimen. This helps to increase the level of confining pressure and accordingly the strength of the rock material in order to reduce compressive damage beneath the projectile. A more complete description of the EOI test can be found in Ref. [21].

In the present experiments, a granite slab of size 200 × 120 × 15 mm^3 is impacted by an aluminum alloy projectile (21 mm in diameter and 40 mm in length) at a speed of 150 m/s. Two tests are performed with similar results and the crack pattern after impact is indicated in Fig. 3.

There are different types of damaged zones in the target with respect to crack density and orientation (see Fig. 3). In the first region (marked (1) in Fig. 3(b)) in front of the projectile there is a small zone consisting of a very large number of cracks in random directions. The material in this region can be considered as crushed due to high compressive stresses beneath the projectile. The second region (marked (2) in Fig. 3(b)) includes a few hoop cracks mostly located close to the confinement. The reason behind the formation of these cracks is not totally clear. However, they presumably form because of wave reflections. The third region (marked (3) in Fig. 3(b)) includes long macroscopic radial cracks, which initiate because of the circumferential motion of the material. The cracks in the second and third region are marked in Fig. 3(b) for the sake of clarity. It is likely that these are mode I cracks initiated by high tensile stresses. In the remaining part of the specimen, outside the above regions, there are an enormous number of cracks, of size up to a few millimeters, in different directions. Most of these cracks are formed along the grain boundaries and some of them are only visible under a microscope. It should be noted that in the region close to the free boundaries, the amount of macroscopic cracks locally increases due to reflections of the compressive wave (spallation).

By observing the surface of the specimen under a microscope, a large number of small cracks can be observed (see Fig. 4). The black color in the micrographs indicates the points where the material is missing, i.e. the cracks. A small part of one of the long macrocracks in Fig. 3(b) is visible in Fig. 4(b), the bold curved line crossing the whole image, together with small cracks oriented in different directions. Note that the amount of damage is decreasing with the distance from the impact point.

In order to evaluate the crack density from the experiment, a line is traced across the micrographs (Fig. 4) and the average distance between the cracks, d, is obtained by dividing the line length by the number of crossed cracks. The crack density is then roughly evaluated as $(1/d)^3$, which in this case is about 1.5×10^9 and 10^9 cracks/m^3 in Fig. 4 (b) and (c) respectively. It should be emphasized that these numbers are rough estimates.

A representative micrograph of the intact specimen is also shown in Fig. 5. A typical feature of the granite material studied herein is the large number of pre-existing cracks, both at the grain boundaries and also across the grains [3], [4]. When compared to Fig. 4, the amount of damage is noticeably increasing after impact.

4.2 Numerical modeling

The equation of motion is discretized using the FE method and the explicit time integration method is employed. The numerical simulation is carried through utilizing in full the KST-DFH material model described above and implemented as a VUMAT subroutine in the Abaqus explicit software [13,28]. The strain increments are given as input whereas final stress tensor and state variables are computed as output variables of the routine. In the subroutine, the integration scheme is mainly composed of two steps. In the first one, a microscopic stress tensor is calculated considering the KST constitutive law alone. The level of pressure is calculated from the volumetric strain increment considering a piece-wise linear relationship between the volumetric strain and the hydrostatic pressure. The microscopic deviatoric stress tensor is

calculated considering the isotropic pressure dependent yield stress criterion defined in Eq. (1). In the second step, the three eigen values of microscopic stress tensor are computed. In case of positive microscopic eigen stresses, a damage variable is calculated according to Eq.(13) and the macroscopic stress is derived (see Eq.(14). Finally, the macroscopic stress tensor is written in the initial basis.

The numerical simulation of the EOI test is performed in 3D. The quarter-symmetry model consists of 8-node linear elements (hexahedra) with reduced integration. The element edge size is 0.5 mm in the rock specimen (see Fig. 6). Surface to surface contact is used in the numerical simulation and all of the KST-DFH model variables are evaluated and extracted during the analysis.

The damage variable, D_1, field is shown in Fig. 7. When the damage variable reaches unity, it indicates that the element is totally damaged, the physical interpretation being that single or multiple cracks normal to the maximum principal stress direction are open. Similar to D_1, the second and third damage components grow during the analysis by increasing the load.

Near the impact point, the material behaves plastically due to high levels of confining pressure. Thus the hydrostatic compressive stresses in this region prevent the fragmentation process. The radial cracks due to hoop tensile stresses induced by the particle motion in the radial direction are also shown in Fig. 7. The compressive stress wave is reflected from the specimen boundaries as a relaxation wave and creates some cracks close to the rear face. Some cracks are also formed due to Rayleigh wave propagation along the free surface of the impact side. It should be emphasized that in the model, crack initiation and growth is solely due to positive principal tensile stresses including the possible contribution from shear stresses. Fracturing due to high compressive stresses (for example in the compacted zone close to the region of impact) is indicated in the model by high values on the accumulated plastic strain.

The crack density, due to the maximum principal stress, predicted by the model is compared to the experimental results. The crack density from the numerical simulation is illustrated in Fig. 8. The results are in logarithmic scale. The crack density in the same region as in Fig. 4 (b) and (c) is about 10^{11} and $10^{10.5}$ crack/m^3 respectively which is higher than the experimental results. This difference will be explained in more detail below.

The number of radial cracks in the numerical results is very large while there are not that many long radial macrocracks visible in the experimental results. This is most likely due to the presence of large so called structural cracks in the specimen introduced during fabrication of the EOI specimen [20]. This feature can indeed be of significant importance for EOI testing of granite as the fabrication of samples requires substantial processing of the material.

To investigate the effect of the structural cracks, the specimen is first impacted at 20 m/s, in a numerical simulation, in order to produce an initial damage. The specimen is subsequently impacted at 150 m/s (similarly as in the experiment). As can be seen in Fig. 9, the damage pattern changes considerably and the number of the radial cracks decreases. The initial cracks prevent some new cracks to form. This effect leads to more realistic results when compared to the experimental observations. The effect of these initial cracks, however, will be further investigated in future studies by introducing these cracks in a more appropriate way. This analysis is only preliminary and leads to a qualitative agreement between experiments and simulations.

Furthermore, the crack density decreases when initial cracking is present and becomes much closer to the experimental results (see Fig. 10). Accordingly, the results shown in Figs. 9 and 10 give some confidence in the present numerical approach and an analysis of percussive drilling is then performed below.

A mesh study for the model is reported by Forquin and Hild before [13]. The boundary between single and multiple fragmentations is affected by the FE size. The smaller the element size, the smaller the region for which multiple fragmentation occurs in the numerical results, because for the same stress rate level, it is more likely for a smaller element to reach failure due to a single crack.

5 Modeling of percussive drilling

The same numerical tools as above are used to model the percussive drilling problem. Again, the KST-DFH material model is utilized *via* a VUMAT subroutine in the Abaqus explicit software [13,28]. A typical drill bit has about ten buttons made of hard steel. To simplify the problem, only one hemispherical button from the bit is considered. Initial damage is not considered in detail as most often in a practical situation there is no preparation of the rock before drilling. Consequently, as discussed previously in the context of the EOI test and in detail in Ref. [20], the formation of large structural cracks should be of less importance. Some simulations relevant to repeated impact are performed. The incident stress pulse has a level of 200 MPa with duration of 2×10^{-4} s and with a rising and descending time of 10^{-5} s. A hemispherical indenter (5 mm in radius) is chosen. The steel drill rod is 1 m in length and 6 mm in radius. In a real tool the drill rod cross sectional area is a bit larger than the sum the cross sectional areas of all buttons. Accordingly, the drill rod radius is taken a bit larger than the button in order to take into account the geometric impedance difference between them. Both the drill rod and the button are assumed to be elastically deformable with elastic moduli equal to 200 GPa and 800 GPa respectively. A block of rock with a size of $200 \times 200 \times 100$ mm^3 is exposed to impact. The finite element mesh used in the simulation is shown in Fig. 11. 8-node linear elements with reduced integration are used in the simulations. Infinite elements are used at the rock boundaries to eliminate the wave reflection.

Selected simulation results for the damage variable, induced by the maximum tensile principal stress, are shown in Fig. 12. Firstly, it is compared to cracking under quasi-static conditions. A typical fracture pattern in a rock material due to quasi-static indentation has been determined by Tan et al.[29] It includes different types of cracks and also a high compressive part under the indenter called the crushed zone, see Fig. 13.

Although being dynamically loaded, similar types of cracks are captured from the numerical results (Fig. 12). In the region ahead of the indenter, a crushed zone develops. The hydrostatic pressure in this region reaches more than 2 GPa according to the numerical results. It should be emphasized that the high hydrostatic stresses will lead to high values on the effective plastic strain and the damage formed in the crushed zone is a consequence of tensile stresses due to a gradual increase of the contact area. Radial cracks, or radial and median cracks combined, are formed during loading and propagate even more during the unloading phase, see Fig. 12(b). Side cracks, which are mainly formed during the unloading stage and are considered as the most efficient way of removing rock material, are also captured. Fig. 14 shows the damage state in a view cut of the rock block 5 mm beneath the indenter at the end of the loading and unloading stages. The side cracks are marked. These cracks interact with similar types from neighboring buttons and a significant part of the material is removed when they coalesce. In this context, it should also

be mentioned that all the three damage variables, in the KST-DFH material model, grow during the simulations.

The penetration resistance is obtained from the indentation bit force (P_b) versus indentation penetration (h) response. The force-penetration (P_b–h) curve of the drill bit is shown in Fig. 15. By accounting for the symmetric boundary conditions and the number of buttons per drill bit, the penetration stiffness, K_s, value is 340 kN/mm. The values of penetration per impact and also the penetration stiffness K_s obtained from the numerical simulations are in good agreement with real drilling results [10].

If the KST model is considered without any damage in the same drilling simulation as above, the penetration rate decreases considerably with a penetration stiffness of about 548 KN/mm, see Fig. 15. This means that in the absence of damage as a dissipation mechanism, the rock behaves as a stronger material and becomes more resistant to the tool indentation.

Mesh size effect on the fracture pattern and the penetration stiffness of the above explained percussive drilling problem have been investigated. It is concluded that the very small details of the crack pattern may be considered as mesh dependent in a sense that the cracks are more likely follow the mesh patterns. However, the size of the damaged zone and the general features of the material response are mainly mesh-independent.

As discussed above, initial damage is not explicitly considered in the present drilling analyses based on the fact that structural cracking is expected to be very limited prior to first impact. It should be emphasized that a controlled introduction of such cracks can be of major importance from a drilling efficiency point of view and, accordingly, this feature will be investigated in detail in future studies. However, as mentioned above, some simulations relevant to repeated impact were performed. In short, it was then found that the cracks formed at first impact continued to grow to a very limited extent while a large zone of crushed material was formed below the indenter leading to a less effective drilling procedure. Based on this result a controlled introduction of structural cracks, in order improve drilling efficiency, becomes an even more desirable feature.

6 Conclusions

Percussive drilling in granite has been investigated experimentally and numerically using finite element simulations. The KST-DFH material model was used to describe the material constitutively and the material parameters are calibrated for Bohus granite by a set of previously performed experiments [20]. The numerical simulations were performed using a VUMAT subroutine in the commercial software Abaqus [13,28].

Edge-On Impact (EOI) tests were performed to validate the numerical model. The fracture pattern and the crack density from the numerical analysis were in qualitative agreement with the experimental results. It was found that effects due to large initial (structural) cracks must be carefully accounted for. These cracks can prevent subsequent initiations and considerably decrease the number of large cracks.

A 3D numerical simulation was then performed to model the percussive drilling problem. It was shown that the fracture pattern at drilling resembles that found under quasi-static indentation of rock materials. In particular, side cracks, which are the most preferable type for removing material, were mainly formed

during the unloading stage. The force-penetration curve and the corresponding value on the penetration stiffness, K_s, were in a good agreement with real drilling data. The possibility of introducing initial cracks in the material, in order to improve the drilling efficiency, was briefly investigated and discussed.

7 References

[1] Saksala T. Numerical Modelling of Rock Fracture in Percussive Drilling. PhD Thesis, Tampere University of Technology, Finland, 2010.

[2] Fang Z, Harrison JP. Development of a local degradation approach to the modelling of brittle fracture in heterogeneous rocks. International Journal of Rock Mechanics and Mining Sciences 2002;39:443–57.

[3] Peng S, Johnson AM. Crack growth and faulting in cylindrical specimens of Chelmsford granite. International Journal of Rock Mechanics and Mining Sciences & Geomechanics Abstracts, vol. 9, Elsevier; 1972, p. 37–86.

[4] Bäckström A, Antikainen J, Backers T, Feng X, Jing L, Kobayashi A, et al. Numerical modelling of uniaxial compressive failure of granite with and without saline porewater. International Journal of Rock Mechanics and Mining Sciences 2008;45:1126–42.

[5] Shimada M, Cho A, Yukutake H. Fracture strength of dry silicate rocks at high confining pressures and activity of acoustic emission. Tectonophysics 1983;96:159–72.

[6] Liu HY, Kou SQ, Lindqvist P-A, Tang CA. Numerical simulation of the rock fragmentation process induced by indenters. International Journal of Rock Mechanics and Mining Sciences 2002;39:491–505.

[7] Wang SY, Sloan SW, Liu HY, Tang CA. Numerical simulation of the rock fragmentation process induced by two drill bits subjected to static and dynamic (impact) loading. Rock Mechanics and Rock Engineering 2011;44:317–32.

[8] Saksala T. Damage–viscoplastic consistency model with a parabolic cap for rocks with brittle and ductile behavior under low-velocity impact loading. International Journal for Numerical and Analytical Methods in Geomechanics 2010;34:1362–86.

[9] Saksala T. Numerical modelling of bit–rock fracture mechanisms in percussive drilling with a continuum approach. International Journal for Numerical and Analytical Methods in Geomechanics 2011;35:1483–505.

[10] Saksala T. 3D numerical modelling of bit–rock fracture mechanisms in percussive drilling with a multiple-button bit. International Journal for Numerical and Analytical Methods in Geomechanics 2013;37:309–24.

[11] Chiang LE, Elias DA. A 3D FEM methodology for simulating the impact in rock-drilling hammers. International Journal of Rock Mechanics and Mining Sciences 2008;45:701–11.

[12] Thuro K, Schormair N. Fracture propagation in anisotropic rock during drilling and cutting. Geomechanics and Tunnelling 2008;1:8–17.

[13] Forquin P, Hild F. A Probabilistic Damage Model of the Dynamic Fragmentation Process in Brittle Materials. Advances in Applied Mechanics 2010;Volume 44:1–72.

[14] Krieg RD. A simple constitutive description for soils and crushable foams. Report, SC-DR-7260883, Sandia National Laboratory 1978.

[15] Swenson D V, Taylor LM. A finite element model for the analysis of tailored pulse stimulation of boreholes. International Journal for Numerical and Analytical Methods in Geomechanics 1983;7:469–84.

[16] Denoual C, Hild F. A damage model for the dynamic fragmentation of brittle solids. Computer Methods in Applied Mechanics and Engineering 2000;183:247–58.

[17] Grange S, Forquin P, Mencacci S, Hild F. On the dynamic fragmentation of two limestones using edge-on impact tests. International Journal of Impact Engineering 2008;35:977–91.

[18] Forquin P, Erzar B. Dynamic fragmentation process in concrete under impact and spalling tests. International Journal of Fracture 2010;163:193–215.

[19] Erzar B, Forquin P. An experimental method to determine the tensile strength of concrete at high rates of strain. Experimental Mechanics 2010;50:941–55.

[20] Saadati M, Forquin P, Weddfelt K, Larsson PL, Hild F. On the mechanical behavior of granite material with particular emphasis on the influence from pre-existing cracks and defects. Report, Department of Solid Mechanics, Royal Institute of Technology (KTH), Stockholm, Sweden: 2013. Submitted for international publication.

[21] Forquin P, Hild F. Dynamic Fragmentation of an Ultr_ahigh-Strength Concrete during Edge-On Impact Tests. Journal of Engineering Mechanics 2008;134:302–15.

[22] Vajdova V, Baud P, Wong T. Compaction, dilatancy, and failure in porous carbonate rocks. Journal of Geophysical Research: Solid Earth (1978–2012) 2004;109.

[23] Weibull W. A Statistical Theory of the Strength of Materials. Report 151, Royal Institute of Technology, Stockholm: 1939.

[24] Weibull W. A statistical distribution function of wide applicability. Journal of Applied Mechanics 1951;18:293–7.

[25] Davies DGS. The statistical approach to engineering design in ceramics. Proc. Brit. Ceram. Soc, vol. 22, 1973, p. 429–52.

[26] Hild F, Billardon R, Marquis D. Hétérogénéité des contraintes et rupture des matériaux fragiles. Comptes Rendus De l'Académie Des Sciences Série 2, Mécanique, Physique, Chimie, Sciences De L'univers, Sciences De La Terre 1992;315:1293–8.

[27] Sallier L, Forquin P. Influence of the Confined Behaviour and the Tensile Strength of Concrete Slabs Under Projectile-Impact. Dynamic Behavior of Materials, Volume 1, Springer; 2013, p. 567–71.

[28] Abaqus 6.11 2011.

[29] Tan XC, Kou SQ, Lindqvist P-A. Application of the DDM and fracture mechanics model on the simulation of rock breakage by mechanical tools. Engineering Geology 1998;49:277–84.

Table legends

Table 1 Parameters used in the KST-DFH material model. Details regarding the parameters are found in Section 2 above.

Mechanical parameters	
E (GPa)	52
ν	0.15
ρ (kg/m^3)	2630
DFH model parameters	
Weibull parameters	
m	23
σ_w (MPa)	18.7
Z_{eff} (mm^3)	195
Obscuration volume parameter	
S	3.74
k	0.38
C (m/s)	4400
KST model parameters	
Parameters for hydrostatic behavior	
K (GPa)	31.7
$\varepsilon_v^{(i)}$	0; -0.028
$P^{(i)}$(MPa)	0; 860
Parameters for deviatoric behavior	
a_0 (MPa^2)	23,500
a_1(MPa)	465
a_2	1.51
Cohesive model parameter	
α_D	1.5
σ_0^d(MPa)	11
ε_0^d	0.004
n_d	1

Table 1

Figure legends

Fig. 1. Quasi-oedometric test results together with the KST model (after [20]).

Fig. 2. Schematic of the EOI test with the sarcophagus configuration.

Fig. 3. Granite specimen after impact by an aluminum projectile (a), damage pattern is marked to be observable (b). Specific regions (1), (2) and (3), are also shown.

Fig. 4. Granit specimen after impact by the aluminum projectile (a), micrograph of the specimen at a distance of 25 mm (b), and 50 mm (c) from the impact point. The dashed yellow boxes will be used to compare the model predictions with the experimentally evaluated crack density.

Fig. 5. Micrograph of the intact specimen.

Fig. 6. FE mesh used in the simulations of the EOI test. Quarter-symmetry model with 775000 8-node linear elements.

Fig. 7. FE simulation results of the EOI test. Damage variable D_1 20 μs (a), and 40 μs (b) after impact (velocity: 150 m/s).

Fig. 8. FE simulation results of the EOI test. Crack density ($1/m^3$, logarithmic scale) due to the maximum principal stress 20 μs (a), and 40 μs (b) after impact (velocity 150 m/s).

Fig. 9. FE simulation results of the EOI test. Damage variable D_1 at the end of the first impact at 20 m/s (a), and 40 μs (b) after the second impact at 150 m/s.

Fig. 10. FE simulation results of the EOI test. Crack density ($1/m^3$, logarithmic scale) due to the maximum principal stress at end of first impact at 20 m/s (a), and 40 μs (b) after the second impact at 150 m/s.

Fig. 11. FE mesh used in the simulations of percussive drilling. Due to symmetries only a quarter of the problem is modeled with 400000 8-node elements.

Fig. 12. FE simulation results of percussive drilling. Damage variable D_1 at the end of loading (a) and at the end of unloading (b) phases.

Fig. 13 Cracking pattern in rocks at quasi-static indentation [29].

Fig. 14. FE simulation results of percussive drilling. Side crack formation in a view cut 5 mm beneath the indenter at the end of loading (a) at the end of unloading (b).

Fig. 15. FE simulation results of percussive drilling. Force-penetration (P_b–h) curve of the drill bit based on the KST-DFH and KST material models.

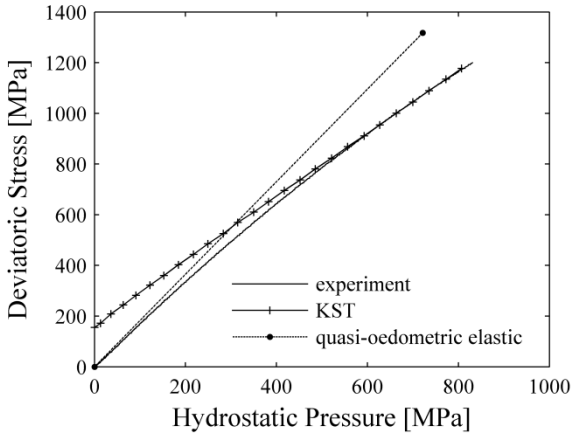
Deviatoric Stress [MPa]
Hydrostatic Pressure [MPa]
0
200
400
600
800
1000
1200
1400
experiment
KST
quasi-oedometric elastic

Fig. 1

‘

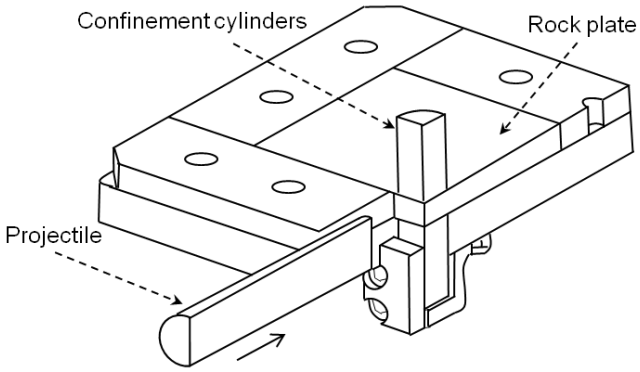

Fig. 2

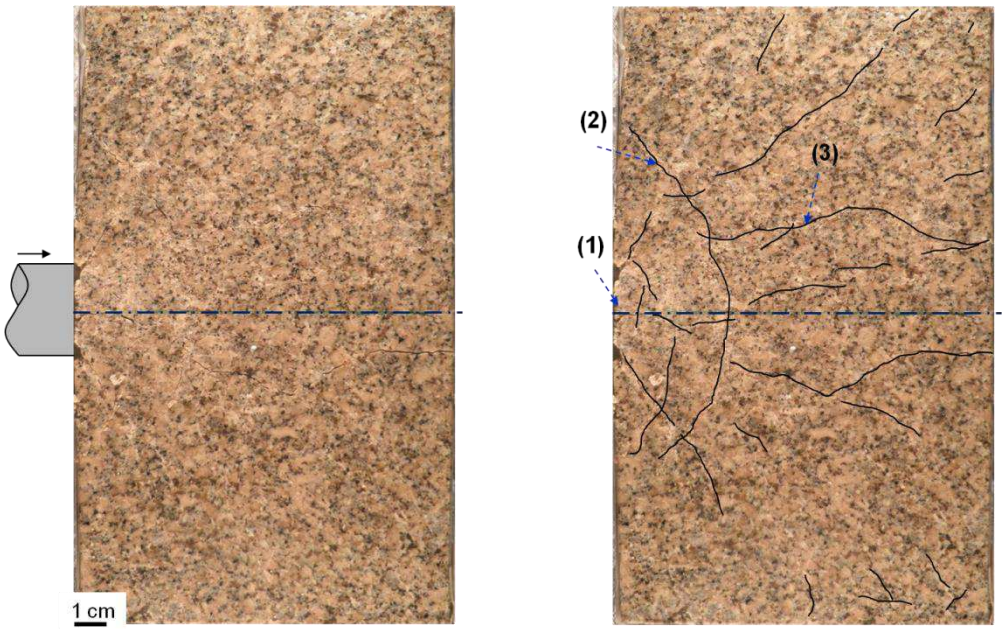

(a) (b)

Fig. 3

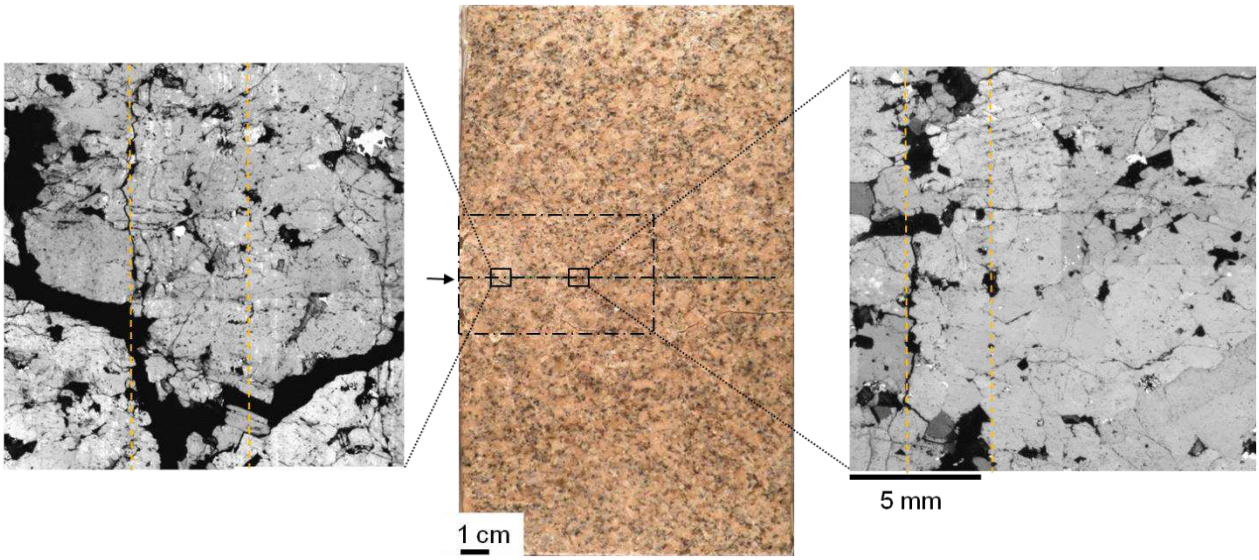

(b) (a) (c)

Fig. 4

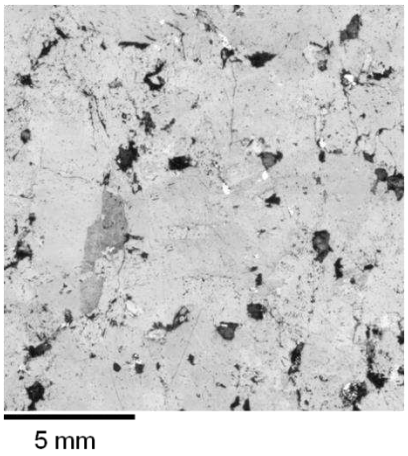

Fig. 5

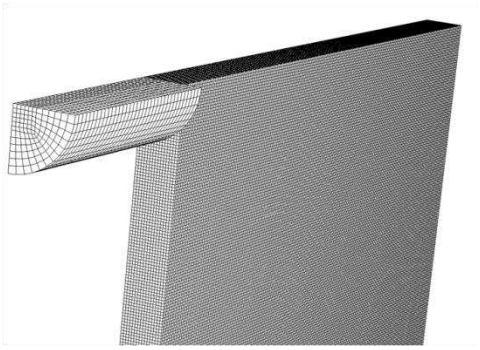

Fig. 6

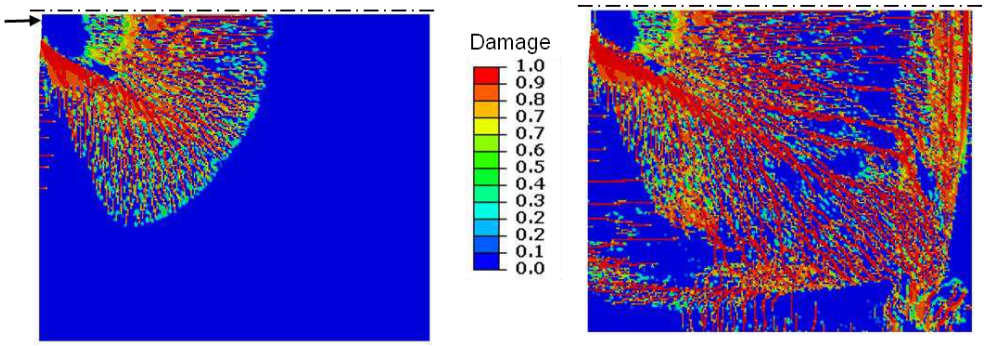

(a) (b)

Fig. 7

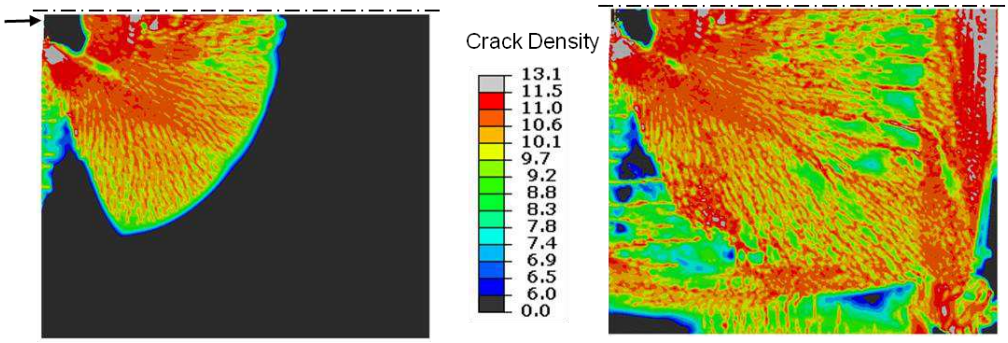

(a) (b)

Fig. 8

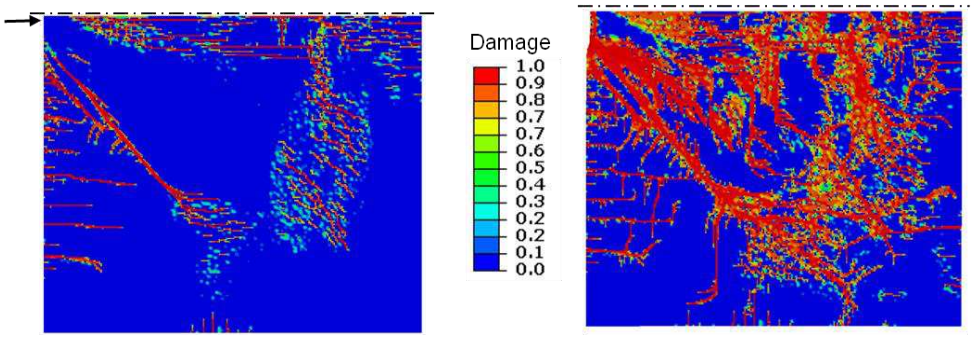

(a) (b)

Fig. 9

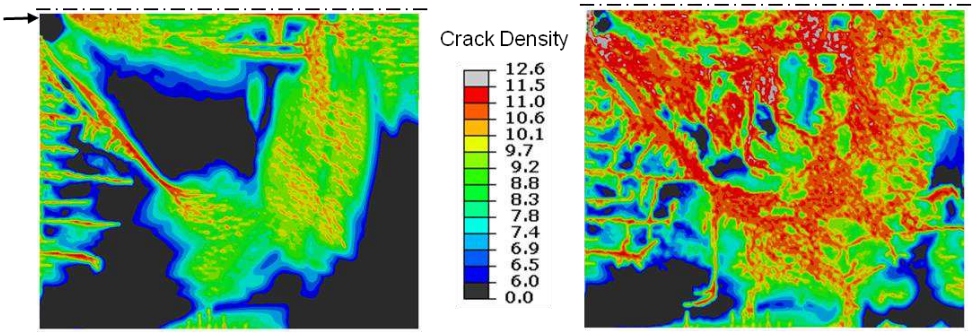

(a) (b)

Fig. 10

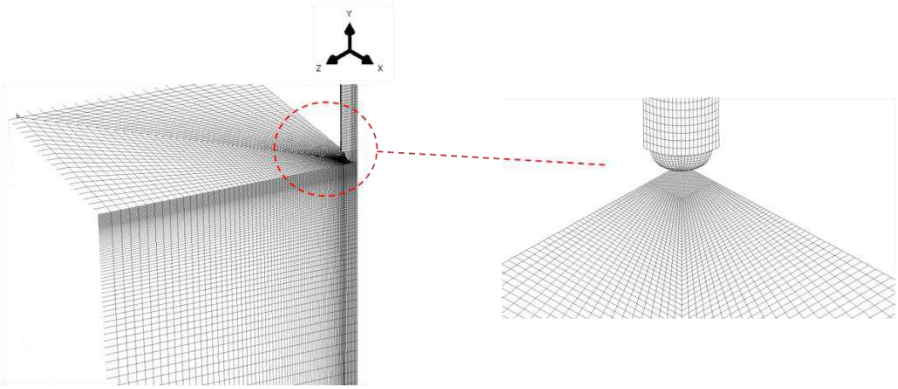

Fig. 11

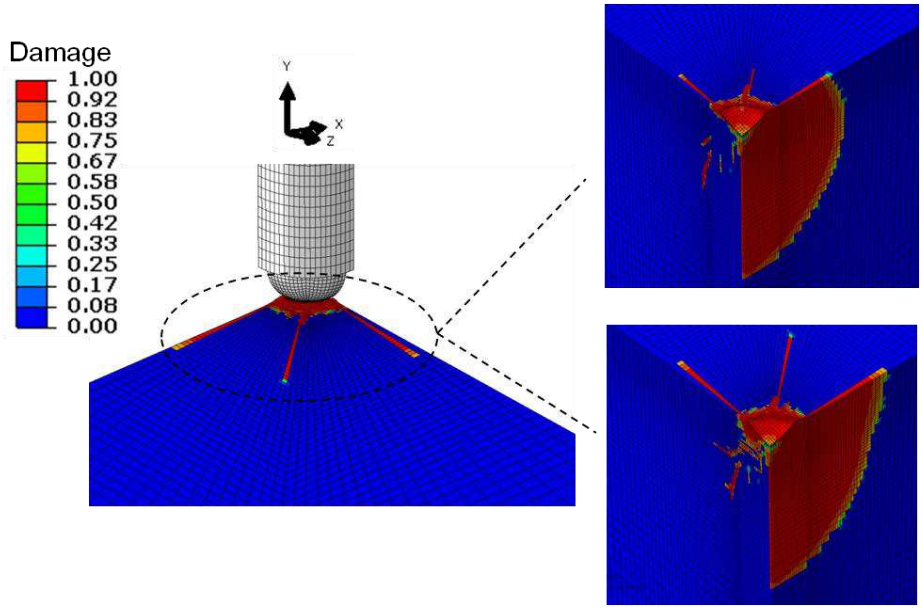

Fig. 12

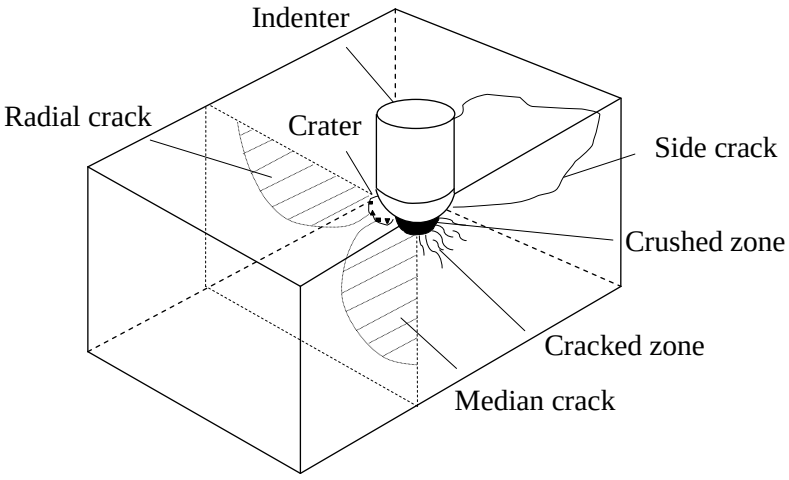
Indenter
Radial crack
Crater
Side crack
Crushed zone
Cracked zone
Median crack

Fig. 13

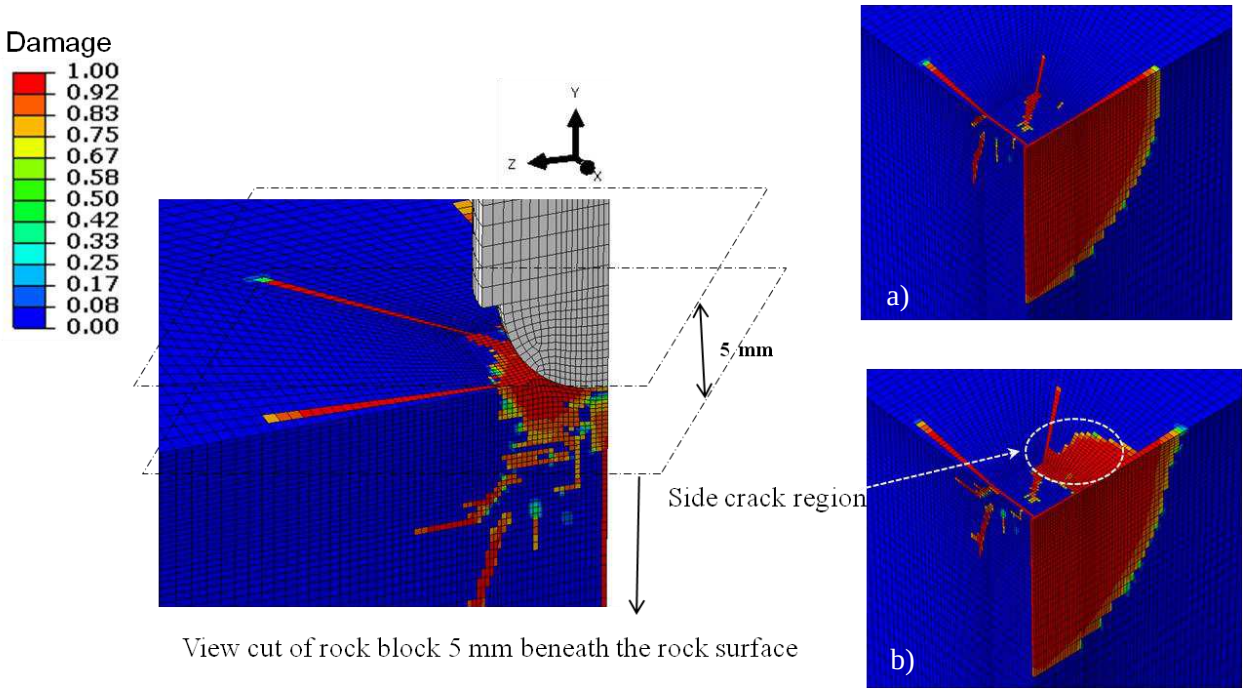
Damage
1.00
0.92
0.83
0.75
0.67
0.58
0.50
0.42
0.33
0.25
0.17
0.08
0.00
Y
Z
X
5 mm
Side crack region
View cut of rock block 5 mm beneath the rock surface
a)
b)

(a) (b)

Fig. 14

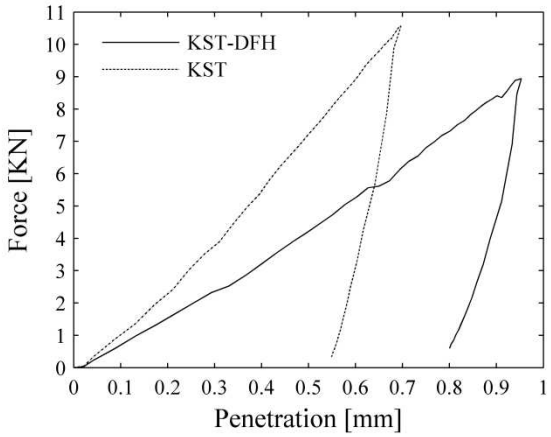
KST-DFH
KST
Force [KN]
Penetration [mm]
0
1
2
3
4
5
6
7
8
9
10
11
0.1
0.2
0.3
0.4
0.5
0.6
0.7
0.8
0.9

Fig. 15